

Systematic Adaptive Robust State Feedback Control for Active Front-End Rectifiers

Aidar Zhetessov, Giri Venkataramanan
UNIVERSITY OF WISCONSIN-MADISON
1415 Engineering Dr.
Madison, WI 53706, United States
Phone: +1 (608) 262-3934
Email: zhetessov@wisc.edu, giri@engr.wisc.com
URL: <https://wempec.wisc.edu/>

Acknowledgments

The authors gratefully acknowledge the members of the Wisconsin Electric Machines and Power Electronics Consortium (WEMPEC) for supporting this work.

Keywords

«Active Front-End», «State-space model», «Small signal stability», «Adaptive control»,
«Robustness».

Abstract

This paper presents the systematic use of physics-based frequency-domain techniques to design the adaptive and robust state-feedback controller for an AFE rectifiers. The proposed design approach ensures robustness and stability of the controller and the converter, independent of the size of the DC-link capacitance. This will enable the optimization of the power circuit from the perspective of efficiency, power density, cost, etc. with the widest possible design space. Furthermore, the control structure is operating-point adaptive, optimally robust and computationally efficient due to closed-form controller representation. Detailed analytical development of the controller is presented in the paper along with a proof for robustness verified using simulations that support the theoretical findings.

1 Introduction

Three-phase six-switch Active Front-End (AFE) rectifiers are the active ac-dc power electronic converters that can be used in various applications to regulate the output dc voltage, keep high ac-side power factor, compensate for the reactive power, or even do primary grid-forming support [1]-[3]. There is an ongoing industrial trend towards constrained multi-objective optimization of power converters, including the AFE rectifiers [4]. One of the major enablers of this trend is the recent advent of wide band-gap (WBG) semiconductor technology [5]. With higher switching frequencies of WBG devices the passive component values can be reduced while preserving the acceptable current/voltage ripple during steady-state operation, thus opening the path towards further passives reduction/optimization [5]. This paper is focused on examining the relationship between the dynamic properties of control of the converter and the size of the reactive components.

While various modulation/control methods have been developed for the AFE rectifiers [2], [7]-[9], conventional cascaded dq-frame PI regulator design has been widely adopted [2], [6]. Furthermore, it is widely known and acknowledged that AFE rectifiers feature a right half plane (RHP) zero arising from its parent boost converter topology. In order to prevent any dynamic instabilities caused by the non-minimal

phase response due to the RHP zero over the complete load range, constraints on passive components sizing were proposed in [6], as reviewed in brief detail in Section 2.

It should be noted that in [6] rather conservative regulator-induced constraints were imposed over and beyond the current/voltage ripple limits on passives even for relatively low switching frequencies. Thus, even at low switching frequencies, the potential for miniaturization of passive components was not properly utilized due to the overly conservative constraints. When higher frequency operation is enabled by WBG devices, such regulator-induced constraints on passive component values would constitute even greater barrier on the path towards system optimization. The goal of the approach presented in this paper is to overcome such constraints through a systematic design of the commonly used cascaded controller structure with an inner current regulator and an outer voltage regulator, illustrated further in Section 3.

While this work preserves the classical control structure it employs various "physics-based" regulator modifications [10]-[12] as detailed in Section 3. Section 4 presents eigenvalue migration of the system with load variation illustrating the designed system stability and adaptability that overcome the dynamic constraints on passive components, along with detailed simulations. Although the evolution of controller parameters is carried out in frequency domain, a parallel viewpoint is taken in Section 5 using state-space modeling, that provides guarantees on overall system robustness, adaptability, transient performance, and computational efficiency. The paper concludes with a section summarizing the contributions.

2 Preliminaries: AFE Rectifier Modeling & Dynamic Constraint

First, we revisit the model of the grid-connected three-phase AFE rectifier, realized as a standard six-switch two-level three-phase topology. An example schematic of the rectifier with resistive load is shown in Fig. 1. Note that in this control-oriented work the AC-side L -filter instead of LCL -filter was considered to focus on control instead of modeling/EMI. The initial nonlinear plant model and electrical parameters are taken from [6]. Table I summarizes the respective specifications, including the minimum DC-link capacitance derived in [6].

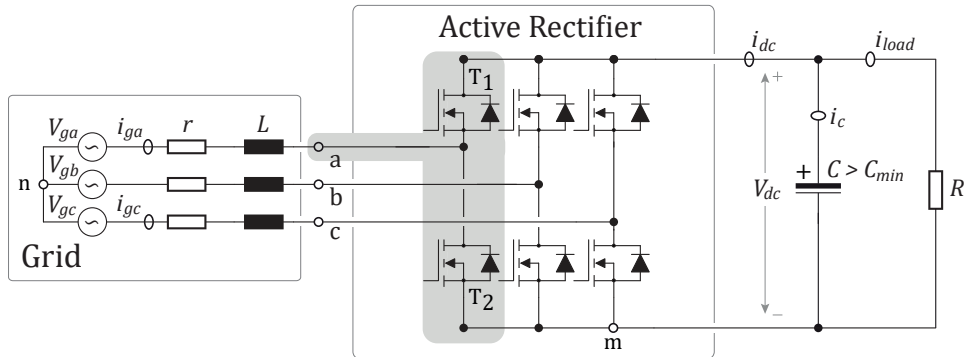


Fig. 1: Active Front End Rectifier Schematic Diagram

Table I: System Specifications and Operating Point Parameters [6]

Parameter	Smbl	Value	Unit	Parameter	Smbl	Value	Unit
AC Input LL RMS Volt.	V_{gLL}	230	Vrms	Sw. Frequency	f_{sw}	10	kHz
DC-bus Voltage	V_{dc}	400	V	Current Ctrl BW*	f_i^*	1	kHz
Rated (Max) Power	P	25	kW	Voltage Ctrl BW*	f_v^*	100	Hz
Rated Load Resist.	R	6.4	Ω	Op. Point d-Crnt	I_{gd}	88.96	A
Grid Frequency	f_o	60	Hz	Op. Point q-Crnt	I_{gq}	0	A
Input Inductance	L	0.34	mH	Op. Point d-Duty	M_d	0.4684	-
Minimum DC Cap [6]	C_{min}	505	μF	Op. Point q-Duty	M_q	-0.0285	-
L Series Resistance	r	5	$m\Omega$	Cmmn-Mode Duty	M_{CM}	0.5	-

After perturbing and linearizing that nonlinear model in dq-frame one can arrive at the following steady-

state operating point relations (1) and state-space plant model (2):

$$M_d V_{dc} = V_{gd} - I_{gd} r, \quad M_q V_{dc} = -\omega_0 L I_{gd}, \quad P = \frac{V_{dc}^2}{R} = \frac{3}{2} (M_d V_{dc} I_{gd}), \quad I_{gq} = 0 \quad (1)$$

$$\begin{aligned} \underbrace{\begin{bmatrix} \dot{\tilde{i}}_{gd} \\ \dot{\tilde{i}}_{gq} \\ \dot{\tilde{v}}_{dc} \end{bmatrix}}_{\dot{x}} &= \underbrace{\begin{bmatrix} -\frac{r}{L} & \omega_0 & -\frac{M_d}{L} \\ -\omega_0 & -\frac{r}{L} & -\frac{M_q}{L} \\ \frac{3M_d}{2C} & \frac{3M_q}{2C} & -\frac{1}{CR} \end{bmatrix}}_{A} \underbrace{\begin{bmatrix} \tilde{i}_{gd} \\ \tilde{i}_{gq} \\ \tilde{v}_{dc} \end{bmatrix}}_x + \underbrace{\begin{bmatrix} -\frac{V_{dc}}{L} & 0 \\ 0 & -\frac{V_{dc}}{L} \\ \frac{3I_{gd}}{2C} & \frac{3I_{gq}}{2C} \end{bmatrix}}_{B_1} \underbrace{\begin{bmatrix} \tilde{m}_d \\ \tilde{m}_q \end{bmatrix}}_{u_1} + \underbrace{\begin{bmatrix} \frac{1}{L} & 0 \\ 0 & \frac{1}{L} \\ 0 & 0 \end{bmatrix}}_{B_2} \underbrace{\begin{bmatrix} \tilde{v}_{gd} \\ \tilde{v}_{gq} \end{bmatrix}}_{u_2} \\ \underbrace{\begin{bmatrix} \tilde{v}_{dc} \\ \tilde{i}_{gq} \end{bmatrix}}_y &= \underbrace{\begin{bmatrix} 0 & 0 & 1 \\ 0 & 1 & 0 \end{bmatrix}}_C \underbrace{\begin{bmatrix} \tilde{i}_{gd} \\ \tilde{i}_{gq} \\ \tilde{v}_{dc} \end{bmatrix}}_x, \quad D = \mathbf{0} \end{aligned} \quad (2)$$

Here the state variables were selected to be small-signal grid dq-frame currents $\tilde{i}_{gd}, \tilde{i}_{gq}$ and DC voltage \tilde{v}_{dc} . The input B matrix was split in two parts to differentiate between manipulated inputs (small-signal modulation indices \tilde{m}_d, \tilde{m}_q) and disturbances (small-signal grid voltage disturbances $\tilde{v}_{gd}, \tilde{v}_{gq}$). $M_d, M_q, I_{gd}, I_{gq} = 0, V_{dc}, V_{gd}$ and $V_{gq} = 0$ are the operating point large-signal parameters, around which the linearization was performed. At nominal conditions and in dq-frame aligned with grid v_{gd} voltage, these steady state parameters are evaluated in Table I. The common-mode duty cycle M_{CM} reflects the steady state voltage between the grid star point and the lower rail of the rectifier. For a standard PWM modulation assumed in this work, the mentioned voltage is kept constant at $V_{CM} = M_{CM} V_{dc} = 0.5 V_{dc}$. This model serves as the case study for the rest of the work. For now, the underlying assumptions of the model are: undisturbed grid voltages, perfect synchronization with grid voltages via PLL, availability of state measurements, perfect knowledge of system parameters, and constant linearized operating point (OP). To be sure, many of these assumptions will be relaxed in the next sections while we evaluate system adaptability and robustness.

Regarding the dynamic constraint, [6] has found the small-signal stability constraint on DC-link capacitance for an AFE rectifier regulated by a conventional cascaded PI control. It turns out that, provided the AC-side inductance $L \geq L_{min}$ (current THD requirement) and maximum power throughput that corresponds to a minimum load resistance R_{min} , the DC-link capacitance should be greater than a minimum value for small-signal stability over the entire load range. That minimum value was derived as follows: $C \geq C_{min} = 20 \cdot L / [M_{d(R_{min})}^2 R_{min}^2]$. Often, in practical designs, the minimum capacitance could be dictated by other requirements such as maximum voltage ripple, ESR, loss, ride-through, etc. However, with the advent of WBG devices, the aforementioned constraints may not be the barriers anymore [5], opening the room for further reduction in capacitor sizing. In fact, as we will see next, even for relatively low switching frequency [6] the minimum capacitance is already dictated by the control-induced constraint above instead of maximum voltage ripple. As f_{sw} goes up this will become even more true, since from voltage ripple standpoint higher f_{sw} requires even smaller C for the same ripple. The following section takes a systematic design approach for the regulator design using various decoupling techniques in order to remove the aforementioned control-induced constraint.

3 Physics-based Controller Design in Frequency Domain

State Feedback (SFB) control method pertains to the linear systems theory and time-domain state-space framework. The state-space framework, although being extremely powerful, might sometimes obscure the physical insight of the control action behind various theorems, eigenpairs, system norms and numerical methods (see next sections). On the other hand, a "physically insightful" controller design techniques have been developed in frequency domain with feedback of state variables, notably for electric machine drives [10]-[12]. This section employs such techniques for the conventional cascaded controller design [6] for the small-signal Frequency Domain (FD) SFB controller. Although the controller design occurs in frequency domain, it is possible to obtain the equivalent state-space representation of the system in order to benefit from both frameworks.

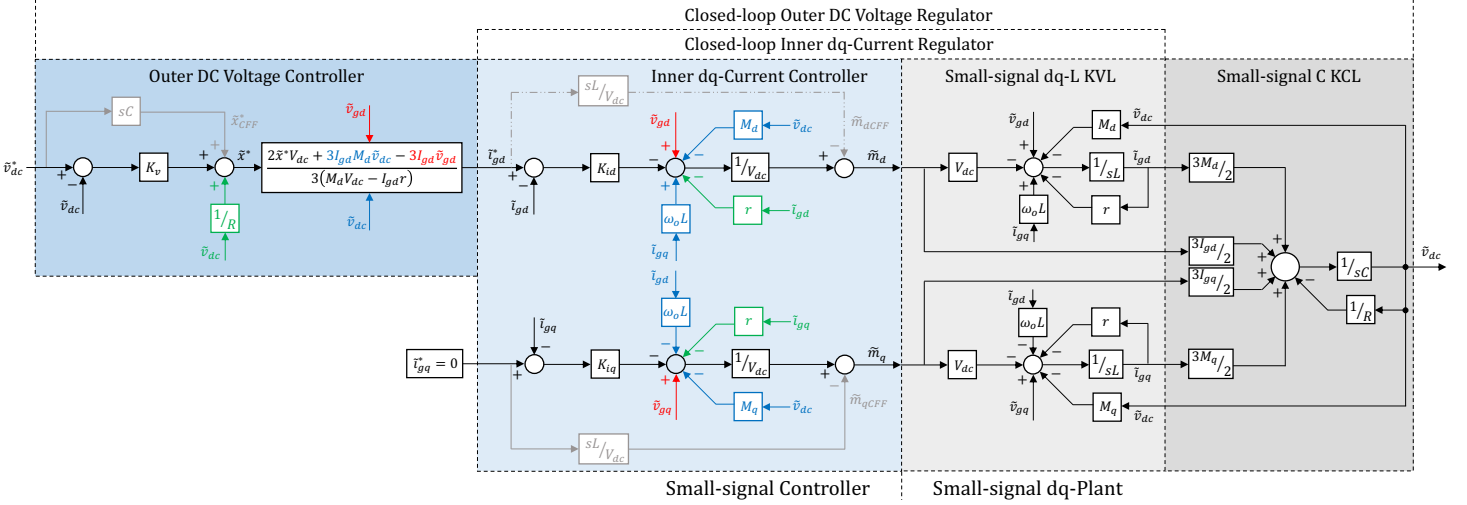


Fig. 2: Block diagram illustrating the augmentations to the classical cascaded controller for the AFE converter using the physics-based techniques: Disturbance Input (DID) / State Feedback (SFBD) / Virtual Zero Reference (VZRD) Decoupling, Command Feedforward (CFF).

The classical cascaded controller (in black) with "physics-based" modifications (in color) for the AFE plant is depicted in the closed-loop block diagram of Fig. 2. In the gray regions on the right one can find the detailed block diagram of the AFE plant small-signal model (2). Unlike the conventional lumped transfer function (TF) representation, the plant block diagram is broken down to its smallest building blocks that provide physical insight. Blue regions on the left are the controller blocks with similar details. The integrator gains were removed from the conventional controller in black due to the SFB nature of the control obviating the need for an integrator [10]. Classical structure uses d- and q-manipulated inputs to regulate d- and q-current components respectively. The q-current reference is zero for unity power factor, while the d-current reference is dictated by the outer cascaded DC voltage controller.

Four frequency domain techniques are used to bring the classical controller to the (optimal) SFB form: Disturbance Input Decoupling (DID), State Feedback Decoupling (SFBD), Virtual Zero Reference Decoupling (VZRD), and the Command Feedforward (CFF). DID attempts to cancel the external disturbances by measuring and applying the same and opposite signals through manipulated inputs. In the AFE case, grid voltage small-signal disturbances could be decoupled as shown in Fig. 2. SFBD attempts to cancel the influence of all other states on the given state dynamics by measuring and applying the same and opposite signals through manipulated inputs. For example, from the plant in Fig. 2 it can be seen that the \tilde{i}_{gd} dynamics are influenced by the \tilde{v}_{dc} through M_d and the appropriate SFBD in blue decouples this effect. VZRD can be regarded as the subset of SFBD, which accounts for the influence of the state itself on its own dynamics. Together, DID, SFBD, and VZRD, starting from the inner-loop towards outer-loop dynamics, simplify the plant such that the respective loop-gain dynamics become first-order and second-order integrators respectively. Those integrator plants can be controlled with near-zero steady state errors using only the proportional gain, hence integrator in controls is redundant. For example, focusing only on the \tilde{i}_{gd} dynamics, DID, SFBD, and VZRD cancel all the influences on \tilde{i}_{gd} , leaving simple $1/sL$ as the (sub)plant to be controlled. By choosing the gain $K_{id} = \omega_i L$, one simply places the closed-loop pole of the inner \tilde{i}_{gd} loop to the desired location ω_i . Finally, CFF accounts for potentially non-constant commands into the respective loops and feeds those forward to the manipulated inputs to ensure the best command tracking (no phase lag and signal attenuation). Inner d-axis CFF may not be easily realizable due to differentiation of measurements coming from outer loop.

Once all the controller modifications of classical PI regulator are made, one can tune the respective cascaded loops to the desired bandwidths that are listed in Table I. Q-axis current loop gain:

$$T_q(s) = \frac{\tilde{i}_{gq}}{(\tilde{i}_{gq}^* - \tilde{i}_{gq})} = \frac{K_{iq}}{sL} \rightarrow K_{iq} = 2\pi f_i L = \omega_i L \quad (3)$$

D-axis cascaded closed-loop TF and gains (assuming perfect decoupling between inner and outer loops):

$$G_d(s) = \frac{\tilde{v}_{dc}}{\tilde{v}_{dc}^*} = \frac{1 - s \frac{I_{gd}L}{M_d V_{dc}}}{\frac{s^2 CL}{K_{id} K_v} + \frac{sC}{K_v} + 1} = \frac{1 - \frac{s}{\omega_z}}{\frac{s^2}{\omega_i \omega_v} + \frac{s}{\omega_i || \omega_v} + 1} \rightarrow K_{id} = (\omega_i + \omega_v)L, K_v = C(\omega_i || \omega_v) \quad (4)$$

Without the assumption above, the TF and gains become OP-dependent ($r \approx 0$, see Table I):

$$\begin{aligned} G_d(s) &= \frac{\tilde{v}_{dc}}{\tilde{v}_{dc}^*} = \frac{1 - s \frac{I_{gd}L}{M_d V_{dc}}}{\frac{s^2 CL}{K_{id} K_v} + s \left(\frac{2L}{K_{id} K_v R} + \frac{2I_{gd}L}{K_v M_d R V_{dc}} + \frac{C}{K_v} - \frac{I_{gd}L}{M_d V_{dc}} \right) + 1} = \frac{1 - \frac{s}{\omega_z}}{\frac{s^2}{\omega_i \omega_v} + \frac{s}{\omega_i || \omega_v} + 1} \\ &\rightarrow K_{id} = \frac{CM_d R V_{dc} (\omega_i + \omega_v) + CI_{gd} L R \omega_i \omega_v - 2M_d V_{dc}}{2I_{gd} + CM_d R V_{dc} L^{-1}}, K_v = LC \omega_i \omega_v K_{id}^{-1}, \omega_z = \frac{M_d V_{dc}}{LI_{gd}} \end{aligned} \quad (5)$$

Finally, multiplying out all the gains for $\tilde{v}_{dc}^* = 0$ in Fig. 2, the manipulated inputs become:

$$\tilde{m}_d = k_{11} \tilde{i}_{gd} + k_{12} \tilde{i}_{gq} + k_{13} \tilde{v}_{dc}, \quad \tilde{m}_q = k_{21} \tilde{i}_{gd} + k_{22} \tilde{i}_{gq} + k_{23} \tilde{v}_{dc} \quad (6)$$

Where the gains k_{ij} , based on the controller gains (5) and Table I specs, are as follows:

$$\begin{aligned} k_{11} &= \frac{K_{id} - r}{V_{dc}} = 5.3545 mA^{-1}, \quad k_{12} = \frac{\omega_o L}{V_{dc}} = 0.3204 mA^{-1} \\ k_{13} &= -\frac{M_d}{V_{dc}} + \frac{2K_{id}V_{dc}[K_v - R^{-1}] - 3K_{id}I_{gd}M_d}{3V_{dc}[M_d V_{dc} - I_{gd}r]} = -1.1458 mV^{-1} \\ k_{21} &= -\frac{\omega_o L}{V_{dc}} = -0.3204 mA^{-1}, \quad k_{22} = \frac{K_{iq} - r}{V_{dc}} = 5.3407 mA^{-1}, \quad k_{23} = -\frac{M_q}{V_{dc}} = 0.0711 mV^{-1} \end{aligned} \quad (7)$$

Given the state-space SFB form ($\dot{\mathbf{x}} = \mathbf{A}\mathbf{x} + \mathbf{B}_1 \mathbf{K}_{fd} \mathbf{x}$), the state-space form of FD controller \mathbf{K}_{fd} is:

$$\mathbf{K}_{fd} = \begin{bmatrix} 5.3545 & 0.3204 & -1.1458 \\ -0.3204 & 5.3407 & 0.0711 \end{bmatrix} \cdot 10^{-3} \quad (8)$$

4 Regulator Evaluation

To evaluate the SFB regulator design above, first, it should be evaluated whether the regulator relaxed the dynamic constraint on DC-link capacitance [6]. For that, one can study only the d-axis closed-loop (CL) system (4-5) - thanks to dq-axes decoupling and stabilizing the q-axis dynamics at the origin. From (5) one can derive the equivalent loop-gain TF, similar to (3):

$$T_d(s) = \frac{\tilde{v}_{dc}}{(\tilde{v}_{dc}^* - \tilde{v}_{dc})} = \frac{\left(\frac{2L}{K_{id} K_v R} + \frac{2I_{gd}L}{K_v M_d R V_{dc}} + \frac{C}{K_v} \right)^{-1} \left(1 - s \frac{I_{gd}L}{M_d V_{dc}} \right)}{s \left[1 + s \left(\frac{2I_{gd}K_{id}}{CM_d R V_{dc}} + \frac{2}{CR} + \frac{K_{id}}{L} \right)^{-1} \right]} \stackrel{(5)}{=} \frac{(\omega_z || \omega_i || \omega_v) \left(1 - \frac{s}{\omega_z} \right)}{s \left[1 + \frac{s}{\omega_i \omega_v} (\omega_i || \omega_v || \omega_z) \right]} \quad (9)$$

From (9) it is seen that two control gains K_{id}, K_v can be used to place the $T_d(s)$ crossover frequency and the open-loop pole to the locations corresponding to the CL voltage/current bandwidths of ω_v, ω_i respectively. Comparing (9) to equations (8)-(10) in [6], one can see that decoupling techniques removed the uncontrolled LHP pole and the integrator zero from the loop gain $T_d(s)$. Recalling that the dynamic constraint arose from the necessary frequency window between the uncontrolled LHP pole and the RHP zero, removing that pole essentially removes the constraint on DC-link capacitance. The RHP zero, being the inherent attribute of the boost-type topologies, is not affected by decoupling. Thus, it is still uncontrollable and still sets the upper bound on the CL bandwidth of the outer-loop voltage regulation.

To further evaluate the designed SFB regulator, closed-loop eigenvalue migration plots and transient simulations can be studied over the load range and for various DC-link capacitance values. For the eigenvalues, the closed-loop system matrices have been derived for both conventional [6] and SFB regulators. The eigenvalues of these matrices were evaluated and plotted (Fig. 3) over the range of DC-link capacitance values and load resistances. The capacitance was swept from the C_{min} value to $0.3C_{min}$, while the load was swept from the rated power $P = 25$ kW to 5 kW (Table I, Fig. 3).

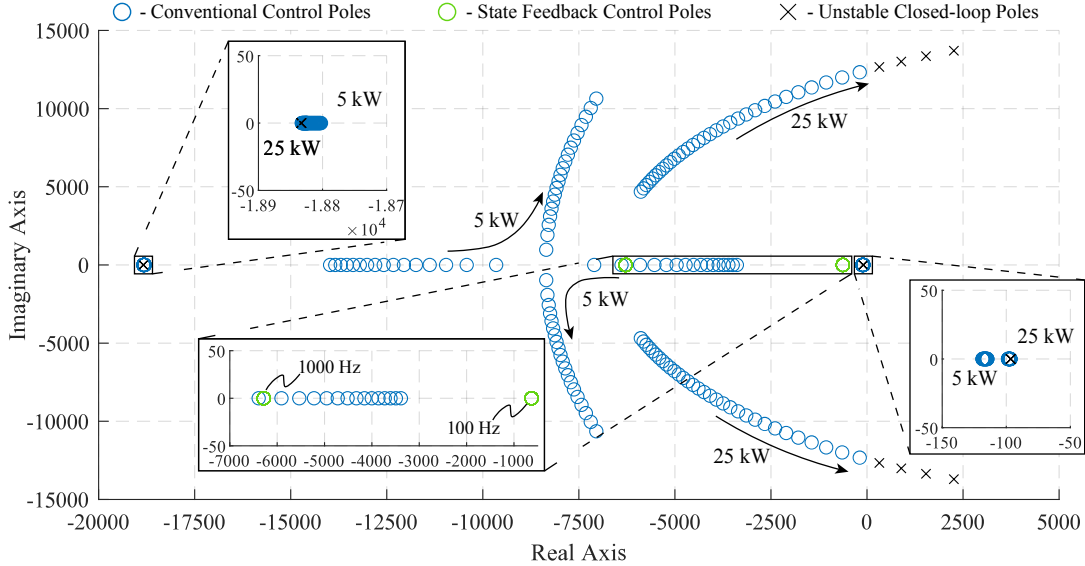


Fig. 3: Effect of DC-link ($C_{min} < C < 0.3C_{min}$) on the closed-loop stability for two control structures/loads.

The conventional system (without any of the decoupling) in Fig. 3 has four distinct CL poles, shown in blue. For 5kW, $C = C_{min}$ conditions, all these poles are along the real axis. When the capacitance is reduced, the poles at the lowest frequency and the highest frequency are relatively stationary. On the other hand, the two of the mid-frequency poles approach each other on real axis and become a complex conjugate pair after meeting each other as the capacitance decreases. For the 25kW case, this pair of poles starts out to be complex, ultimately leading to instability (RHP poles) at $C = 0.3C_{min}$, as predicted by [6]. On the other hand, the SFB system has only two distinct CL poles, that are shown in green. This is expected, as the desired CL bandwidths for both current loops were selected to be the same - 1 kHz (6.28 krad/s). The third pole of the voltage loop is located at 100 Hz (628 rad/s). Notably, the CL eigenvalues with the proposed controller using (7) are stationary irrespective of capacitance and/or load variation, provided that capacitance and load values are known.

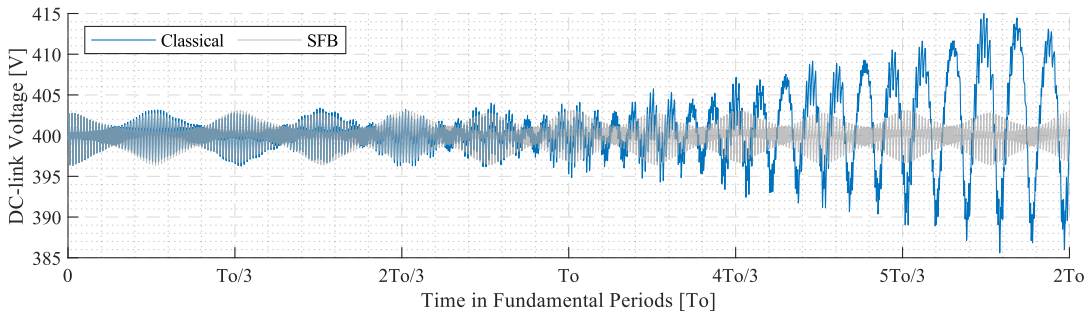


Fig. 4: Switched model simulation results for DC-link voltage at $C = 0.5C_{min}$ and Classical [6]/SFB controls.

A detailed simulation of the system using the switched nonlinear model was developed to verify the approach presented in the paper. Fig. 4 illustrates the dc bus voltage for conventional control (blue) and the proposed control (gray), illustrating the effective stabilization of the unstable operating condition. Looking at the gray waveform, note how small the voltage ripple envelope is - only $\pm 3V$ peak, which is less than 1% for a dc voltage of 400V. Recalling from Table I that simulated $f_{sw} = 10\text{kHz}$, one can

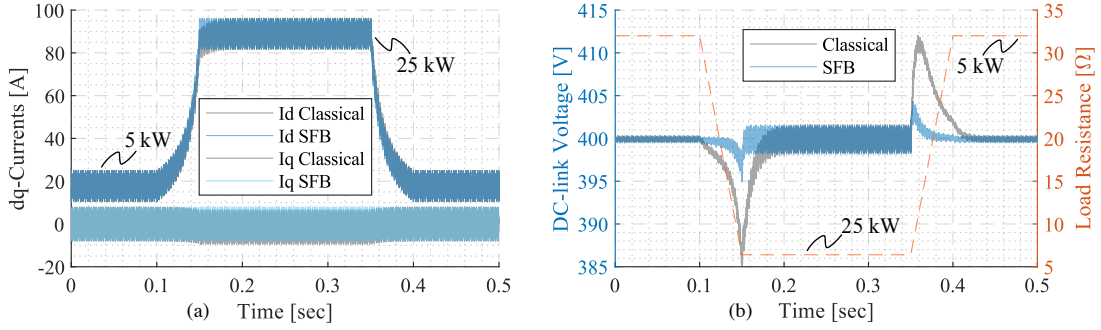


Fig. 5: Transient simulation results for (a) dq-axes currents, and (b) DC-link voltage for Classical and SFB controls. The R_{load} changes between 32Ω (5 kW) and 6.4Ω (25 kW). Capacitance value: $C = C_{min}$.

get an idea how large the simulated capacitance of $0.5C_{min}$ is. Indeed, even at such a low switching frequency the voltage ripple is still very small, implying unnecessarily large DC-link capacitance value. From voltage ripple perspective $0.5C_{min}$ is too large, yet from stability perspective we see that classical CL system (blue) is unstable, requiring even more capacitance for stability. As f_{sw} increases, this gap between voltage ripple and stability constraints is set to increase even further. Thus, one can see the importance of a proper control system - it "unleashes" the advantages of high switching frequency in passive component minimization (power density, efficiency, cost etc).

In addition to small-signal stability at reduced capacitance values, the designed SFB controller improves the transient system performance even for larger C values, without compromising the stability of conventional control. Fig. 5 shows large-signal transient simulation scenario where the load is rapidly varied between 5 and 25 kW. The capacitance is kept at $C = C_{min}$. It can be seen that for all three state variables of interest (i_{gd}, i_{gq}, v_{dc}) the transient overshoot, settling time, and command tracking are improved.

5 Insights on Robustness & Adaptability

So far the work addressed the SFB controller designed in frequency domain (FD). However, as it was mentioned, the SFB control originally pertains to the State-Space (SS) framework. The SS framework has the controller design tools that, provided controllability of the system, can place the closed-loop (CL) eigenvalues to any desired locations. In addition, if there are degrees of freedom (DOFs) in feedback matrix \mathbf{K}_{ss} , the tools can use those to achieve the desired characteristics. For instance, the numerical algorithm behind Matlab PLACE command uses the DOFs to minimize the upper bound on sensitivities of CL poles to small perturbations in \mathbf{A} and \mathbf{B}_1 , thus maximizing small-signal robustness [13]-[14].

An interesting insight is found when applying Matlab PLACE tool to place the CL eigenvalues of the AFE rectifier system to $\Lambda = [\lambda_1, \lambda_2, \lambda_3] = [2\pi \cdot 1000, 2\pi \cdot 1000, 2\pi \cdot 100]$ (Table I):

$$\dot{\mathbf{x}} = \mathbf{Ax} + \mathbf{B}_1 \underbrace{(-\mathbf{K}_{ss}\mathbf{x})}_{\mathbf{u}_1} \rightarrow \mathbf{K}_{ss} = \text{PLACE}(\mathbf{A}, \mathbf{B}_1, \Lambda) = \begin{bmatrix} 5.3545 & 0.3204 & -1.1458 \\ -0.3204 & 5.3407 & 0.0711 \end{bmatrix} \cdot 10^{-3} \quad (10)$$

Here $\mathbf{K}_{ss} \in \mathbb{R}^{2 \times 3}$ is a SS SFB controller matrix that moves the CL eigenvalues of the state dynamics to the desired locations. Comparing the controllers in (8) and (10), one can see that they are identical for the operating point (OP) at hand. Other OPs (other load resistances) were also evaluated, and the observed alignment holds true for those OPs as well. Therefore, at least for the AFE case, FD SFB controller gives identical results as the SS SFB controller generated numerically using PLACE tool. Method [13] maximizes small-signal robustness using the control DOFs. Moreover, the numerical method minimizes the upper bounds on the norm of the feedback matrix and transient response (minimal control effort and transient peaks), and maximizes the lower bound on stability margin. For the proofs of these statements refer to [13]-[14]. Since the FD SFB controller is identical to the SS SFB one, it retains all the advantages above, while also being in an explicit closed-form.

Gaining a bit more insight into the small-signal robustness of "physics-based" SFB controls, [14] derives the upper bound on CL eigenvalue sensitivity as:

$$\frac{d\lambda_{i \in \{1..n\}}}{d\varepsilon} \leq n \cdot \kappa_2(\mathbf{X}) \equiv n \cdot \|\mathbf{X}\|_2 \cdot \|\mathbf{X}^{-1}\|_2, \text{ where } \mathbf{X} \in \mathbb{C}^{n \times n} - \text{matrix of CL right eigenvectors} \quad (11)$$

Here $\kappa_2(\mathbf{X})$ is the *spectral condition number* of the CL matrix $\mathbf{A}_{cl} = \mathbf{A} + \mathbf{B}_1 \mathbf{K}$, ε is the small-signal perturbation of any entry in \mathbf{A}_{cl} , n is the number of states. $\kappa_2(\mathbf{X})$ is always greater or equal to 1 and it gets to its unique minimum ($=1$) when \mathbf{A}_{cl} is a normal matrix (all of its CL normalized eigenvectors \mathbf{X} are orthogonal to each other - orthonormal eigenvector condition). From physics perspective, the CL eigenvectors \mathbf{X} are orthogonal when the state dynamics are decoupled from each other and that is exactly what the "physics-based" techniques aim for - they do physics-informed decoupling actions for plant simplification and control. Thus, it turns out that "physics-based" decoupling techniques can result in an optimally robust CL SFB system, at least for the AFE rectifiers.

Theoretical insight above relates only to the small-signal robustness, or CL eigenvalue sensitivity to parameter variations (11). To assess the effect of greater parameter variations, switched model simulations and/or Lyapunov functions [16] can be used. For simulations, consider the same transient scenario as in Fig. 5, but with $L = 2 \times L$ and $C = 0.8 \times C_{min}$ as an example of unmodeled large parameter variation in the plant. Fig. 6a shows the transient waveforms of the system states in such scenario. It is seen that classical PI CL system (gray) becomes unstable at high power (low load resistance), while the SFB CL system (blue) preserves stability. Note that lack of integrator in control leads to a very small steady-state error in DC-link voltage and grid currents even for significant parameter variations. Slow integrators can be added to the outer loops to eliminate steady state error completely.

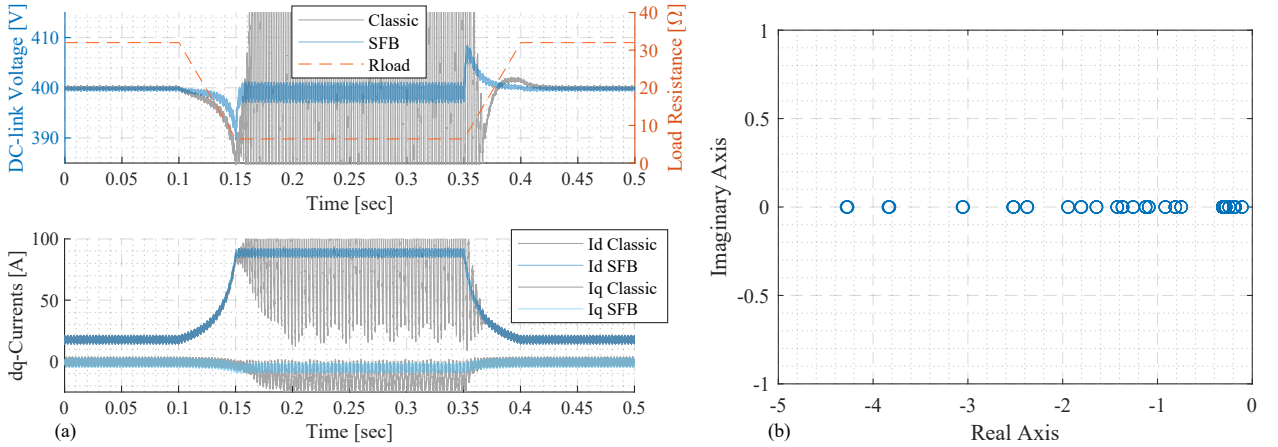


Fig. 6: Transient robustness simulation (a) for dq-axes currents and DC-link voltage for Classic and SFB controls. The R_{load} is swept 32Ω (5 kW) - 6.4Ω (25 kW). Parameter variation: $C = 0.8 \cdot C_{min}$, $L = 2 \cdot L$. Eigenvalue sweep (b) of the Lyapunov derivative matrix $\mathbf{A}_{cl}^\top(t)\mathbf{P} + \mathbf{P}\mathbf{A}_{cl}(t)$ for $0.5 \cdot L \rightarrow 2 \cdot L, 0.5 \cdot r \rightarrow 2 \cdot r$ parameter variations.

As of Lyapunov functions, one can use some results for linear time-varying (LTV) systems to evaluate the system robustness at any given OP more precisely. For a CL LTV systems with certain bounds on parameter variations in $\mathbf{A}_{cl}(t)$, one can conclude asymptotic stability of the system irrespective of the temporal nature of parameter variations within the defined bounds, if there exists a positive-definite Lyapunov function $V(\mathbf{x})$ with a negative-definite time derivative for all possible $\mathbf{A}_{cl}(t)$ [16].

Consider $2 \times$ parameter variations in L and r due to thermal/saturation/proximity effects for example. Since L, r enter the system matrices \mathbf{A} and \mathbf{B}_1 , entries of those will change, affecting $\mathbf{A}_{cl}(t) = \mathbf{A}(t) + \mathbf{B}_1(t)\mathbf{K}$. As those variations are not modeled, the controller matrix will not change. Robust asymptotic stability of the system in such conditions can be concluded if there exists $\mathbf{P} = \mathbf{P}^\top > 0$ such that:

$$V(\mathbf{x}) = \mathbf{x}^\top \mathbf{P} \mathbf{x} > 0, \quad \dot{V}(\mathbf{x}) = \mathbf{x}^\top (\mathbf{A}_{cl}^\top(t)\mathbf{P} + \mathbf{P}\mathbf{A}_{cl}(t))\mathbf{x} < 0, \quad \forall \mathbf{x} \neq 0, \quad \forall t \quad (12)$$

Inspired by solution of $\dot{V}(\mathbf{x}) = -\mathbf{x}^\top \mathbf{I}\mathbf{x}$, one can get the following energy-like Lyapunov matrix \mathbf{P} :

$$\mathbf{P} = \begin{bmatrix} \frac{L}{2} & 0 & \frac{\sqrt{LC}}{4}; & 0 & \frac{L}{2} & 0; & \frac{\sqrt{LC}}{4} & 0 & \frac{C}{2} \end{bmatrix} = \mathbf{P}^\top > 0 \quad (13)$$

The range of parameters of interest ($0.5 \cdot L \rightarrow 2 \cdot L, 0.5 \cdot r \rightarrow 2 \cdot r$) was swept with high resolution to evaluate the negative-definiteness of $\mathbf{A}_{cl}^\top(t)\mathbf{P} + \mathbf{P}\mathbf{A}_{cl}(t)$ in each case by checking the respective eigenvalues. From Fig. 6b one can see that all eigenvalues throughout the sweep are strictly negative, implying robust asymptotic stability of the system at the peak power OP in the presence of large L, r parameter variations.

Moving on to adaptability, it is enabled by the fact that, unlike the output of numerical optimization, the designed regulator is in the closed-form (7). Studying (7) and the control gains (3), (5) therein, it is seen that the regulator depends on AFE parameter estimations (L, C, r), PLL output ω_o , and OP large-signal quasi-steady-state parameters ($M_{dq}, I_{gdq}, V_{dc}, R = V_{dc}/I_{load}, V_{gdq}$). The CL robustness to AFE parameter variations has already been shown above. ω_o is the measurement coming from the PLL. The OP parameters can be obtained from measurements and OP relations (1) - see the example below.

For example, $V_{dc} = V_{dc}^*$, I_{gd} can be obtained from low-pass filtering the i_{gd} measurement. The low-pass filter frequency used in this work was $f_v^*/10$ to separate the high-frequency ripple content from the low-frequency quasi-steady-state OP part ($i_{gd} = I_{gd} + \tilde{i}_{gd}$). Similarly one can obtain $I_{load}, R, V_{gdq}, \tilde{V}_{gdq}, \tilde{V}_{dc}$. There are no measurements for M_{dq} , but those can be calculated from (1). The combined manipulated input (duty cycles) would then become: $m_{dq} = M_{dq} + \tilde{m}_{dq}$ - large-signal part M_{dq} and small-signal part \tilde{m}_{dq} (Fig. 2). Note how the manipulated input comprises large- and small-signal parts.

Having shown how the OP parameters can be obtained from measurements in real time, one can now see how the SFB regulator is made adaptive. Indeed, since the SFB control gains (7) explicitly depend on measurable OP parameters, SFB gains will change with OP variation - load step, AC voltage change etc.

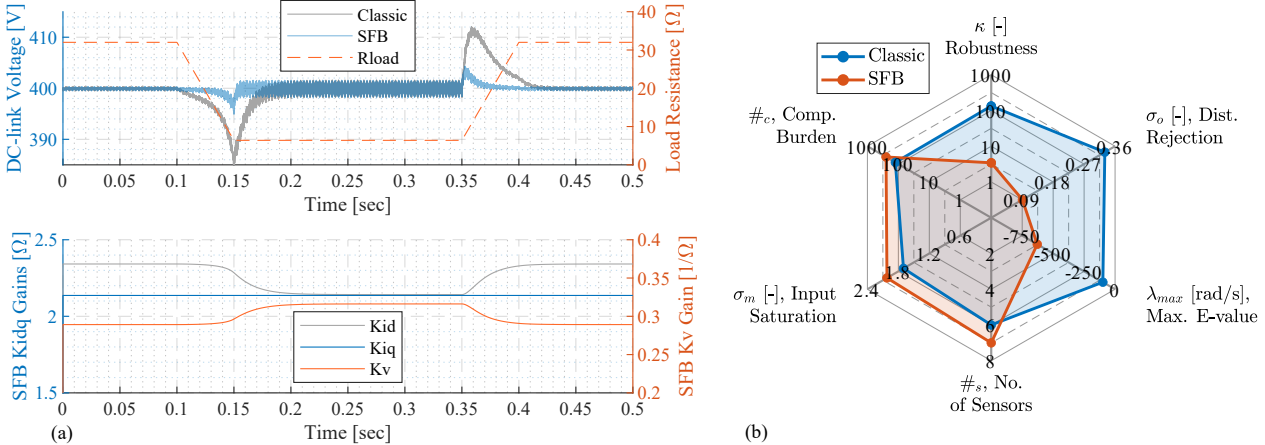


Fig. 7: Transient adaptability simulation (a) for DC-link voltage for Classical and SFB controls. The R_{load} changes between 32Ω (5 kW) and 6.4Ω (25 kW). SFB control gains K_{id}, K_{iq}, K_v adapt to OP variation. Comparative evaluation (b) of the control structures using spider plot of performance metrics. Smaller hexagon - better performance.

To support the claims on adaptability, Fig. 7a shows the same dc voltage transient as in Fig. 5. Also, it plots the control gains that were used in real time during the transient. The gains are derived from (3), (5) using OP parameter measurements. Indeed, it is seen that the control gains do change based on OP. Moreover, adaptive SFB control results in a better transient performance - less over/undershoot, settling time etc., in addition to aforementioned robustness and reduced capacitance capability.

With the obtained robustness and adaptability, the systematically designed SFB AFE regulator at hand retains the same CL eigenvalues at any OP, does not overload the small-signal controller with large-signal measurements, while also preserving optimal performance at any given OP without numerical optimization. Hence the name of the paper - systematic adaptive robust SFB control for AFE rectifiers.

To highlight various aspects of the designed SFB versus classical regulator, Fig. 7b depicts the comparative evaluation spider diagram. The diagram aims to evaluate and compare various small-signal performance metrics of controllers to explicitly see the pros and cons of SFB/classical controllers applied to the same AFE rectifier plant given in Table I. Generally, the smaller the diagram area the better the overall controller performance.

Six axes indicate the performance metrics evaluated. κ - measure of small-signal robustness, CL eigenvalue sensitivity of the normalized (unitless) CL matrix \mathbf{A}_{cl} (11). σ_o, σ_m - measures of small-signal disturbance rejection and small-signal input saturation, disturbance-to-output and disturbance-to-manipulated input normalized (unitless) peak singular values, also known as \mathcal{H}_∞ -norms [15]. λ_{max} - measure of small-signal transient convergence, maximum (the least negative) real-part CL eigenvalue. $\#_s, \#_c$ - measures of sensor requirement and computational burden, number of sensors and number of multiplication/addition operations made by controller in simulation within one switching period.

It can be seen from Fig. 7b that the designed SFB controller has much better small-signal robustness, disturbance rejection and transient convergence. All these come at the cost of slightly increased computational burden, input saturation and one more sensor (load current). With these one can claim superiority of SFB over the classical controller for the nominal AFE plant. The SFB advantage grows even further when capacitance reduction and adaptability are taken into account.

6 Conclusion

With recent proliferation of WBG semiconductors and higher switching frequencies, there is a trend towards passives' miniaturization in power converters. Although higher switching frequencies enable even smaller passive components to provide satisfactory ripple values during steady state, more subtle dynamic stability constraints still put a lower bound on passive component values even for low switching frequencies, as it was shown for AFE rectifiers with cascaded control. This work attempts to remove the aforementioned dynamic constraints for three-phase six-switch two-level AFE rectifiers by modifying the conventional control through physics-based frequency-domain techniques.

It turns out from the analysis and simulations that within the bandwidth, dictated by the RHP zero of the rectifier, the reported dynamic constraint on AFE DC-link capacitance was removed by the designed regulator - smaller DC-link capacitance values can be used compared to previous literature.

Interesting observation leading to numerous conclusions is that analytically-designed state-feedback controller of this paper is the same as the one obtained numerically in [13]. The controllers are precisely the same over the full load range. Moreover, the numerically obtained controller guarantees maximum robustness for closed-loop eigenvalues, minimum upper bound on the norm of the feedback matrix (minimal control action) and transient response, as well as maximum lower bound on stability margin. Equality of the analytical and numerical controllers implies 1) that the analytically designed SFB controller retains all the guarantees of the numerical solution; and 2) that utilized analytical controller design techniques might constitute a generalized design methodology for a robust power electronics controllers based on physical insight. Validating the second implication above requires more studies in the future.

Finally, the work proposed how to make the designed robust controller operating point-aware by explicitly splitting the measurements into the operating point large-signal part and the rippy small-signal part using low-pass filters. Combined with the fact that the designed controller is analytical (in the closed-form), the system can achieve robust behavior in an operating-point-adaptive fashion without numerical optimization for every operating point. This approach to adaptability is not constrained to the AFE, implying that it also might constitute a generalized adaptability methodology for the linearized nonlinear systems. Again, validating this implication requires a deeper dive into control systems theory.

References

- [1] R. Teodorescu, M. Liserre and P. Rodriguez, Grid converters for photovoltaic and wind power systems. Chichester, U.K.: Wiley, 2011, pp. 1-4.

- [2] Y. Yin et al., "Adaptive Control for Three-Phase Power Converters With Disturbance Rejection Performance," in IEEE Transactions on Systems, Man, and Cybernetics: Systems, vol. 51, no. 2, pp. 674-685, Feb. 2021.
- [3] Q.-C. Zhong and Z. Lyu, "Droop-Controlled Rectifiers That Continuously Take Part in Grid Regulation," IEEE Transactions on Industrial Electronics, vol. 66, no. 8, pp. 6516-6526, 2019.
- [4] J. W. Kolar and T. Friedli, "The essence of three-phase pfc rectifier systems - part i," IEEE Transactions on Power Electronics, vol. 28, no. 1, pp. 176-198, 2013.
- [5] H. A. Mantooth, M. D. Glover and P. Shepherd, "Wide Bandgap Technologies and Their Implications on Miniaturizing Power Electronic Systems," in IEEE Journal of Emerging and Selected Topics in Power Electronics, vol. 2, no. 3, pp. 374-385, Sept. 2014.
- [6] B. Shi, G. Venkataraman, and N. Sharma, "Design consideration for reactive elements and control parameters for three phase boost rectifiers," in IEEE International Conference on Electric Machines and Drives, 2005, pp. 1757-1764.
- [7] M. P. Kazmierkowski and L. Malesani, "Current control techniques for three-phase voltage-source PWM converters: a survey," in IEEE Transactions on Industrial Electronics, vol. 45, no. 5, pp. 691-703, Oct. 1998.
- [8] B. Singh, B. N. Singh, A. Chandra, K. Al-Haddad, A. Pandey and D. P. Kothari, "A review of three-phase improved power quality AC-DC converters," in IEEE Transactions on Industrial Electronics, vol. 51, no. 3, pp. 641-660, June 2004.
- [9] Hengchun Mao, C. Y. Lee, D. Boroyevich and S. Hiti, "Review of high-performance three-phase power-factor correction circuits," in IEEE Transactions on Industrial Electronics, vol. 44, no. 4, pp. 437-446, Aug. 1997.
- [10] M. J. Ryan, W. E. Brumsickle and R. D. Lorenz, "Control topology options for single-phase UPS inverters," in IEEE Transactions on Industry Applications, vol. 33, no. 2, pp. 493-501, March-April 1997.
- [11] F. B. del Blanco, M. W. Degner and R. D. Lorenz, "Dynamic analysis of current regulators for AC motors using complex vectors," in IEEE Transactions on Industry Applications, vol. 35, no. 6, pp. 1424-1432, Nov.-Dec. 1999.
- [12] F. Briz, M. W. Degner and R. D. Lorenz, "Analysis and design of current regulators using complex vectors," in IEEE Transactions on Industry Applications, vol. 36, no. 3, pp. 817-825, May-June 2000.
- [13] J. Kautsky, N. K. Nichols, and P. Van Dooren, "Robust pole assignment in linear state feedback," International Journal of Control, vol. 41, pp. 1129-1155, 1985.
- [14] J. Wilkinson, Algebraic eigenvalue problem. Oxford: Clarendon Press, 1965, pp. 87-90.
- [15] S. Skogestad and I. Postlethwaite, Multivariable Feedback Control: Analysis and Design. Chichester, U.K.: Wiley, 2010, pp. 537-538.
- [16] K. Gu, M. A. Zohdy and N. K. Loh, "Necessary and sufficient conditions of quadratic stability of uncertain linear systems," in IEEE Transactions on Automatic Control, vol. 35, no. 5, pp. 601-604, May 1990, doi: 10.1109/9.53534.